



HAL
open science

Black Silicon Revisited as an Ultrabroadband Perfect Infrared Absorber over 20 μm Wavelength Range

Sreyash Sarkar, Ahmed Elsayed, Yasser Sabry, Frédéric Marty, Jérémie Drévilon, Xiaoyi Liu, Zhongzhu Liang, Elodie Richalot, Philippe Basset, Elyes Nefzaoui, et al.

► **To cite this version:**

Sreyash Sarkar, Ahmed Elsayed, Yasser Sabry, Frédéric Marty, Jérémie Drévilon, et al.. Black Silicon Revisited as an Ultrabroadband Perfect Infrared Absorber over 20 μm Wavelength Range. *Advanced Photonics Research*, 2023, 4 (2), pp.2200223. 10.1002/adpr.202200223 . hal-04044980

HAL Id: hal-04044980

<https://hal.science/hal-04044980v1>

Submitted on 17 Jul 2023

HAL is a multi-disciplinary open access archive for the deposit and dissemination of scientific research documents, whether they are published or not. The documents may come from teaching and research institutions in France or abroad, or from public or private research centers.

L'archive ouverte pluridisciplinaire **HAL**, est destinée au dépôt et à la diffusion de documents scientifiques de niveau recherche, publiés ou non, émanant des établissements d'enseignement et de recherche français ou étrangers, des laboratoires publics ou privés.



Distributed under a Creative Commons Attribution 4.0 International License

Black Silicon Revisited as an Ultrabroadband Perfect Infrared Absorber over 20 μm Wavelength Range

Sreyash Sarkar, Ahmed A. Elsayed, Yasser M. Sabry, Frédéric Marty, Jérémie Drévilon, Xiaoyi Liu, Zhongzhu Liang, Elodie Richalot, Philippe Basset, Elyes Nefzaoui, and Tarik Bourouina*


Black silicon properties are investigated in the wavelength range extending from 0.2 to 25 μm with a focus on the mid-infrared (MIR). It is demonstrated that concurrently increasing the initial level of doping of bare silicon, with given limits, enables reaching even higher absorptance and higher spectral range. Unprecedented light absorptance levels are obtained on black silicon with up to 99.5% in the spectral range from 1 to 8 μm and above 90% until 20 μm , leading to ultrabroadband, ultrablack silicon surfaces. The synergetic effects of morphology and volume doping are elucidated; in particular, how the high aspect-ratio of conical nanostructures plays a crucial role. The experimental findings are analyzed with numerical simulations involving plasmonic effects of highly doped silicon and supported by tomographic processing of microscopy images. Guidelines and corresponding manufacturing routes are provided by which ultrabroadband, ultrablack silicon surfaces can be obtained within minutes of plasma processing, with no need for further functionalization. With the scalable manufacturing involving solely pure silicon, the resulting ultrabroadband perfect absorbers should be of benefit for large-scale deployment of radiative cooling devices, blackbody infrared light sources, and infrared radiation sensing.

1. Introduction

While bare single-crystal silicon already occupies a dominant position in semiconductor industry, its format involving surface microscale/nanostructuring is still of prime intrigue regarding its optical properties for a variety of applications such as solar cells,^[1–3] radiative cooling,^[4–7] black body radiation sources,^[8,9] photodetectors,^[10–12] and infrared absorbers.^[13–15] These applications require at least low reflectance and, more often than not, they also require high absorptivity, which translates into high emissivity, according to Kirchhoff's law of thermal radiation.^[16] To achieve these functions, various micro/nanogeometrical shapes have been implemented on silicon surfaces like periodic cylindrical pillars or disordered conical spikes. These are also referred to in the literature as silicon nanowires (SiNWs)^[17–20] or black silicon (B-Si),^[21–50] respectively. B-Si is among the most popular nanostructured surfaces. Its name is due to its appearance to the bare eye, and it is known to absorb light mainly in the visible wavelength range, up to nearly 1 μm , owing to bandgap absorption

S. Sarkar, A. A. Elsayed, F. Marty, X. Liu, E. Richalot, P. Basset, E. Nefzaoui, T. Bourouina
Univ Gustave Eiffel
CNRS
ESYCOM
Marne la Vallée F77454, France
E-mail: tarik.bourouina@esiee.fr

Y. M. Sabry
Electronics and Electrical Communications Department
Faculty of Engineering
Ain Shams University
Cairo 11517, Egypt

 The ORCID identification number(s) for the author(s) of this article can be found under <https://doi.org/10.1002/adpr.202200223>.

© 2022 The Authors. Advanced Photonics Research published by Wiley-VCH GmbH. This is an open access article under the terms of the Creative Commons Attribution License, which permits use, distribution and reproduction in any medium, provided the original work is properly cited.

DOI: 10.1002/adpr.202200223

J. Drévilon
Institut Pprime, CNRS
Université de Poitiers
ISAE-ENSMA
Futuroscope Chasseneuil, 86360, France

X. Liu
School of Optoelectronic Science and Engineering
Soochow University
Suzhou 215006, China

X. Liu, Z. Liang
Changchun Institute of Optics, Fine Mechanics and Physics
Chinese Academy of Sciences
Changchun, Jilin 130033, China

X. Liu
Fondation de l'Ecole Normale Supérieure
Paris 75005, France

combined with its particular morphology. B-Si can be produced by various techniques, including femtosecond laser irradiation,^[11–28] chemical etching,^[2] or plasma surface treatment^[10,29–33] as considered in this work. Compared with flat silicon, B-Si generally exhibits a much higher absorptivity and hence a much higher emissivity. **Table 1** summarizes the most significant achievements in state-of-the-art of research conducted on B-Si expressed with the corresponding absorptivity or reflectivity and corresponding spectral range.

Alternative strategies to achieve perfect light absorbers and emitters, that is, nonsilicon black absorbers, include surface functionalization with MoS₂,^[51] graphene,^[52] or with colloidal metallic nanoparticles.^[53,54] Another option is to design metacells along silicon-based metamaterials.^[13–15,55] Among these strategies, the most effective to date are the use of metallic nanoparticles, which exhibit plasmonic behavior over a broad spectral range as reported by Zhou et al.,^[53,54] reaching up to 99% absorptivity over a spectral range of 10 μm.

Compared to the abovementioned nonsilicon black absorbers, B-Si has the advantage of preserving the integrity of the silicon substrate because there is neither additional coating nor functionalization in this case. B-Si appears as a good candidate for light absorbers based solely on silicon. Nevertheless, even though

some B-Si surfaces exhibit extremely high absorption of nearly 99% of incident light in the visible and near-infrared (NIR) range,^[21–27,30–33,41–46] only meager information is available in mid-infrared (MIR) and far-infrared spectral ranges^[28,47,48] (bottom part of Table 1). The limited investigations in the infrared range could be due to a negative a priori that silicon is a translucent material in the infrared, which makes it a priori not a very good candidate for a good absorber in the infrared wavelength range. As an illustration, **Figure 1a,b** shows typical spectral reflectance responses on black silicon, as found in many reports covering the visible and NIR ranges up to 2.5 μm; most of the time, such curves show a decrease of the absorptance at the highest wavelengths at the limits of bandgap absorption around $\lambda = 1 \mu\text{m}$, after what bare silicon turns into a translucent material to the infrared. This kind of drop also suggests that absorption should deteriorate even more if one increases the wavelength further. A nice evidence of such a transition step at the border between visible and NIR was reported many times in the earliest history on black silicon.^[21–24,32,46,49,50] However, some of these reports have also shown an improvement of the absorptance above 1 μm, which appears in **Figure 1a,b** as a reduction of the magnitude of the absorption step at $\lambda = 1 \mu\text{m}$. This improvement was ascribed to the virtues of doping the silicon surface, which can be seen also as a kind of surface functionalization. Doping the silicon surface with sulfur, selenium, or tellurium with subsequent laser treatment led to absorptance up to 80% till 2.5 μm.^[46] But it was also found that such improvement is not stable with temperature,^[22] as illustrated in **Figure 1b**, which shows that the effect of thermal annealing brings back a high step and lowers the absorptance above 1 μm. Similar to surface doping, a functionalization of the surface of black silicon with gold nanoparticles led to an absorptance up to 96% till 2.5 μm.^[49] More recently, boron volume doping led to an increase of the absorptance up to 99.8% until 2.25 μm.^[32] It is worth mentioning that those reports on doping black silicon did not explore wavelengths above 2.5 μm. It is also worth mentioning that the effects of doping on the extension of spectral range were ascribed to the introduction of intermediate energy states in the semiconductor bandgap,^[22] which is questionable as discussed in this article, in which we introduce a simple explanation based on the plasmonic behavior of doped silicon, along a model based on a simple Drude model adapted to structured silicon, which is proven to fit very well with experimental data, with no need for more sophisticated models such as the Drude–Lorentz model for instance.

Volume doping of bare silicon was already identified as a candidate for tailoring thermal radiative properties^[56] by taking benefit of the plasmonic effects exhibited by doped silicon^[57] at lower plasma frequencies compared to metals, lying in the NIR range. On the other hand, although it was not considered as a plasmonic material, heavily boron-doped, degenerated silicon was already used to manufacture B-Si with enhanced absorptance^[32] in the NIR up to 2500 nm (group 4 on **Figure 1c**). Extending these properties further to the MIR range is of primary importance for the numerous abovementioned applications.

In the present article, we investigate absorption properties of B-Si in the infrared spectral range up to $\lambda = 25 \mu\text{m}$, at variable doping levels and different nanostructured features. Surprisingly, excellent absorptance is found, reaching 99.5%

Table 1. Radiative properties of black silicon absorbers in literature. Majority of absorptance data are obtained by the indirect method, through measurements of reflectance and transmittance spectral responses. Among these data, only a few values (*) take into account diffuse reflectance, meaning that majority of absorptance values are overestimated. Only one work use a direct method to provide data on emissivity (**). For the purpose of comparison, the data related to this work are provided with (and without) consideration of diffuse reflectance.

| References | Explored wavelength range $\lambda_{\text{min}}-\lambda_{\text{max}}$ [μm] | Minimum reflectance R [%] | Maximum absorptance A [%] |
|-----------------------------------|--|---------------------------|---------------------------|
| Algasinger et al. ^[41] | 0.2–1.1 | 4 | – |
| Branz et al. ^[42] | 0.3–1.1 | 2 | – |
| Nguyen et al. ^[30] | 0.4–0.95 | 1 | – |
| Pezoldt et al. ^[43] | – | 2 | – |
| Repo et al. ^[40] | – | 1 | – |
| Kontermann et al. ^[25] | – | 2 | – |
| Steglich ^[33] | – | 1 | – |
| Atteia et al. ^[44] | – | 0.2 | 99* |
| Yurasov et al. ^[45] | 0.5–1.2 | 3 | 97 |
| Steglich et al. ^[32] | 0.25–2.25 | – | 99.8* |
| Tull et al. ^[46] | 0.8–2.5 | – | 95 |
| Wu et al. ^[22] | 0.3–2.5 | – | 97 |
| Crouch et al. ^[24] | 0.3–2.5 | – | 97 |
| Ma et al. ^[26] | 0.4–2.5 | – | 90 |
| Li et al. ^[27] | 0.25–2.5 | – | 96 |
| Vorobyev et al. ^[28] | 1–15 | 20 | – |
| Liu et al. ^[47] | 1.5–16.5 | 5 | 90 |
| Maloney et al. ^[48] | 2.5–25 | – | 90** |
| This work | 1–25 | 0.6* (0.03) | 99.5* (99.97) |

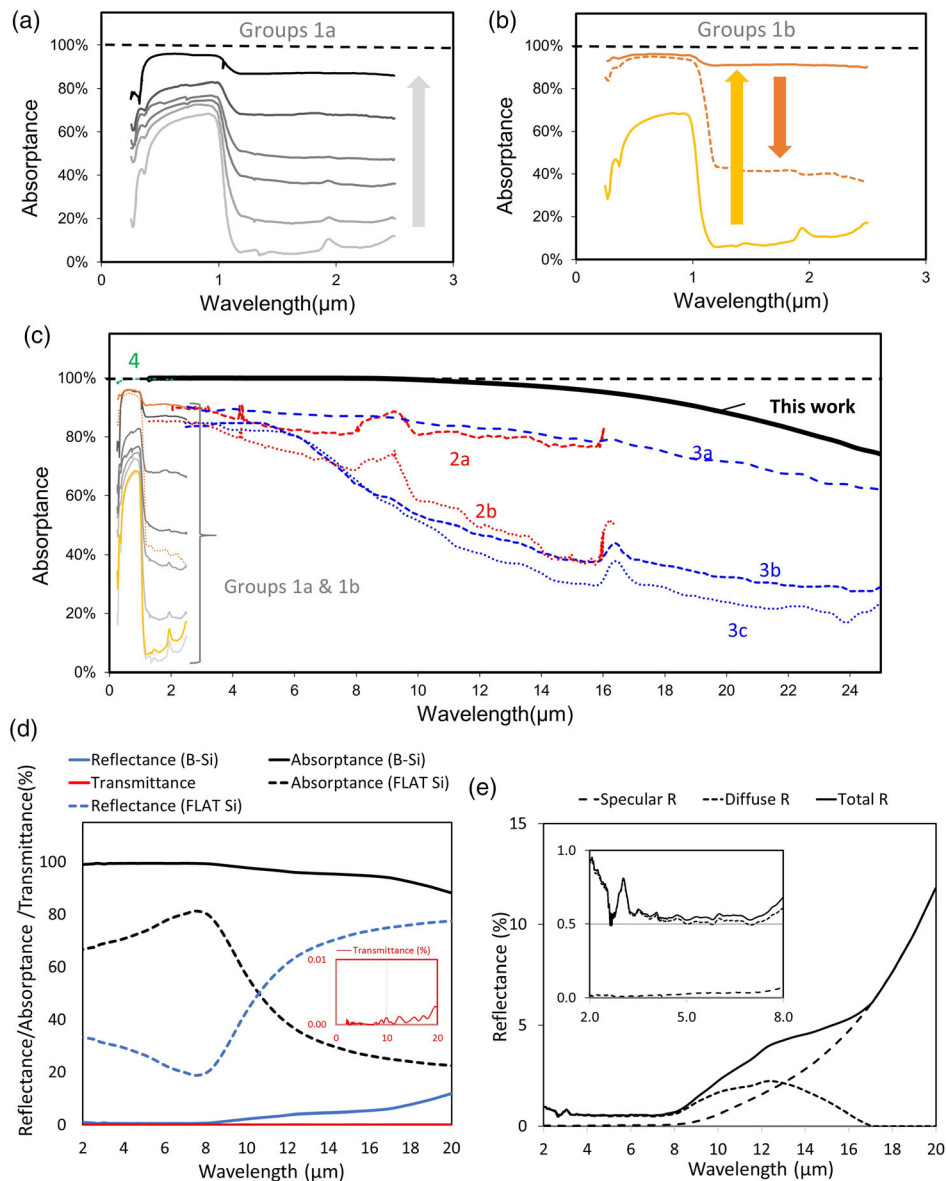


Figure 1. Absorptance of B-Si: state-of-the-art and comparison to this work. a,b) Absorptance up to $\lambda = 2.5 \mu\text{m}$ wavelength of sulfur-doped B-Si surfaces showing a drop at $\lambda = 1.1 \mu\text{m}$, corresponding to the silicon bandgap. a) Group 1a adapted from Crouch et al.,^[24] SF_6 -assisted laser etching with different number of laser pulses from 0 to 500. b) Group 1b adapted from Wu et al.,^[22] SF_6 -assisted laser etching with different etching depths of $0 \mu\text{m}$ (bottom curve), $10\text{--}12 \mu\text{m}$ (top curve) then after annealing (dotted-line curve). c) Absorptance up to $\lambda = 25 \mu\text{m}$; this work (upper thick black curve); group 2, adapted from Liu et al.,^[47] relates to SF_6 -assisted laser etching with different etching depths: 2a ($20\text{--}30 \mu\text{m}$) and 2b ($3\text{--}4 \mu\text{m}$); group 3, adapted from Maloney et al.,^[48] relates to different surface dopants: 3a (S), 3b (Te), and 3c (Se); group 4, adapted from Steglich et al.,^[32] boron-doped B-Si up to $\lambda = 2.5 \mu\text{m}$. d) This work: details of reflectance and transmittance data used to determine the absorptance of our B-Si-1 sample (phosphorous volume doping with concentration of $5 \times 10^{19} \text{cm}^{-3}$ and etched depth of $10.3 \mu\text{m}$); the inset shows a zoom on transmittance, much below 0.005%. Dashed lines relate to measured data on a flat Silicon wafer with the same doping level e, the corresponding detailed data for B-Si of specular reflectance, diffuse reflectance, and total reflectance for our B-Si-1 sample.

up to $8 \mu\text{m}$ and still above 90% up to $20 \mu\text{m}$. Figure 1c shows this result shown in the thick black curve, compared to the best absorptance spectra reported in the literature so far, in the same wavelength range.^[32,47,48] This result was reached while considering simultaneously high doping of the silicon bulk and high

aspect ratio nanostructures at its surface, prompting ultrabroad-band ultrablack silicon (UB-B-Si) over a spectral range fully covering the UV, visible, and NIR but also the MIR, toward the borders of far-infrared. A comprehensive experimental study has been conducted and is supported by numerical simulation

results obtained with different modeling techniques, namely, the finite element method (FEM) and the effective medium theory^[58] (EMT) combined with the transfer matrix method^[59] (TMM). The shapes and dimensions of morphological features of B-Si are also considered for better understanding the important role of nano- and microstructures in enhancing light absorption. Considering different doping levels, numerical results on B-Si are discussed and compared with flat silicon used as a reference. In all cases, numerical and experimental results show a very good agreement, indicating the key role of doping together with the strong importance of geometrical features in the morphology of B-Si, namely, the shape and aspect ratio of the nanostructures, for obtaining outstanding radiative properties. Our analysis yields crucial information regarding an effective pathway to obtaining ultrabroadband absorption silicon using conventional microelectronics industry tools.

In what follows, we will present and discuss our results that reveal how a bare single-crystalline silicon surface can be tailored to exhibit ultrahigh absorptivity, but also how such high absorptivity can be extended to an ultrawide spectrum extending to the borders of far-infrared. We show and explain that the overall behavior is critically governed by two factors, 1) morphology and 2) doping, with the requirement to properly control both of them simultaneously. Those two factors are studied in detail.

2. Results and Discussion

The measured infrared absorptance (A) is obtained from the indirect method (i.e., $A = 1 - R - T$) based on measured transmittance (T) and reflectance (R) spectra accounting for both specular reflection and diffuse reflection (see Section 4.3 for experimental details). The spectral responses for A , R , and T of the fabricated B-Si are shown in Figure 1d,e. A resulting absorptance of 99.5% is obtained in the spectral range up to $\lambda = 8 \mu\text{m}$ (this result is also drawn in the upper thick black curve in Figure 1c so as to compare it with state-of-the-art). The data given in Figure 1e show the detailed fractions of diffuse reflectance and specular reflectance contributing to the total reflectance. They are nearly 0.5% and 0.03%, respectively, in the spectral range up to $\lambda = 8 \mu\text{m}$. As shown in the inset of Figure 1d, the transmittance remains much below 0.005% in the whole spectral range up to $\lambda = 20 \mu\text{m}$. It is worth mentioning that such negligible transmittance measured through the highly doped silicon substrate also implies that one can get the absorptance directly from the simplified relation $A \approx 1 - R$. From $\lambda = 8 \mu\text{m}$ up to $20 \mu\text{m}$, absorptance decreases but remains at nearly 90%. It is worth mentioning that it is mainly due to the specular reflectance in this range as can be seen from Figure 1e, not by diffuse reflectance. Figure S1, Supporting Information 1, gives complementary information about the absorptance of our surfaces in the spectral range starting from $\lambda = 0.2 \mu\text{m}$ up to $2.5 \mu\text{m}$, which is near-unity over the whole range, in particular with no discontinuity at the bandgap limit at $\lambda = 1 \mu\text{m}$ contrary to the typical responses recalled in Figure 1a,b. Considering the data of both Figure S1, Supporting Information, and Figure 1b, one has the demonstration of the extension from $0.2 \mu\text{m}$ up to $20 \mu\text{m}$ of the UB-B-Si.

2.1. Effect of Morphology

2.1.1. Effect of Structures' Depth

A first effect of the morphology can be seen in the measured spectral responses shown in Figure 2a, which relates to three distinct nanostructured surfaces with conical shapes having different average depths $\langle d \rangle$ but same doping level of $5 \times 10^{19} \text{cm}^{-3}$ (N-type, phosphorous doping). The first sample B-Si-1 with $\langle d \rangle = 10.3 \mu\text{m}$ maintains a remarkable absorptance of nearly 95% till a wavelength $\lambda = 17 \mu\text{m}$ as shown by the black curve. For the second sample B-Si-2, having a lower depth value of $\langle d \rangle = 4.3 \mu\text{m}$ (green curve), the drop from the 95% absorptance ceiling occurs progressively at shorter wavelengths below $\lambda = 9 \mu\text{m}$. A flat surface is also measured as reference, corresponding to the ultimate situation of $\langle d \rangle = 0.0 \mu\text{m}$ (red curve).

For a better understanding of these first experimental results, we made FEM simulations, Supporting Information 2, as shown in Figure 2b, where the average depth was gradually varied from $\langle d \rangle = 0 \mu\text{m}$, corresponding to a flat surface up to $\langle d \rangle = 10 \mu\text{m}$. For these simulations, we considered a lateral correlation length, that is the mean spacing between neighboring cones, $L_c = 0.3 \mu\text{m}$ and an angle of incidence of 15° for the incident electromagnetic plane wave, same as in the experimental conditions. We performed those simulations on simplified models where the doped silicon material was considered as a plasmonic material, which can be described by a wavelength-dependent complex refractive index based on Drude's Model, Supporting Information 3. Such model is used as an input for various electromagnetic simulations to compute the surface radiative properties over the $1\text{--}25 \mu\text{m}$ wavelength range. The set of curves of Figure 2a,b illustrates, through experiments and simulations, the same clear trend: with larger depth $\langle d \rangle$, a broader and higher level of absorptance is reached. The ultimate limit of 100% absorptance is made possible across a wide infrared wavelength range up to $\lambda = 8 \mu\text{m}$, and 95% is maintained up to $\lambda = 15 \mu\text{m}$, while the absorptance is still above 90% at $\lambda = 20 \mu\text{m}$. It is noteworthy that this requires micro-nanostructure depths $\langle d \rangle$ as big as $10 \mu\text{m}$, also corresponding to the order of magnitude of the cutoff wavelength, defined here as the wavelength at which the absorptance falls below 99%, suggesting that one needs a depth $\langle d \rangle \approx \lambda$ to achieve a smooth-enough transition from air to bulk silicon without reflection. Both experimental and simulation results highlight this requirement of a very high aspect ratio for the conical structures, translating in this case in a rather important depth in the order of $\langle d \rangle \approx 10 \mu\text{m}$. This is indeed a first key requirement for a broadband perfect absorption. It is worth mentioning that this is a singularity of our ultrablack silicon to reach such high aspect ratio cones in the order of 30:1, with subwavelength width, while the vast majority of B-Si surfaces exhibit a much smaller aspect ratio in the order of 3:1. The high aspect ratio and highly doped black silicon appear as an efficient taper metasurface, preventing any reflection to occur over a wide wavelength range. The transmitted light by this taper metasurface is then fully absorbed by the tandem resulting from this metasurface and the underlying thick substrate, which is also highly doped. Figure 2c shows the simulated spectral absorptance when varying the correlation length (L_c) from 0.1 to $0.5 \mu\text{m}$, showing multiple superimposed

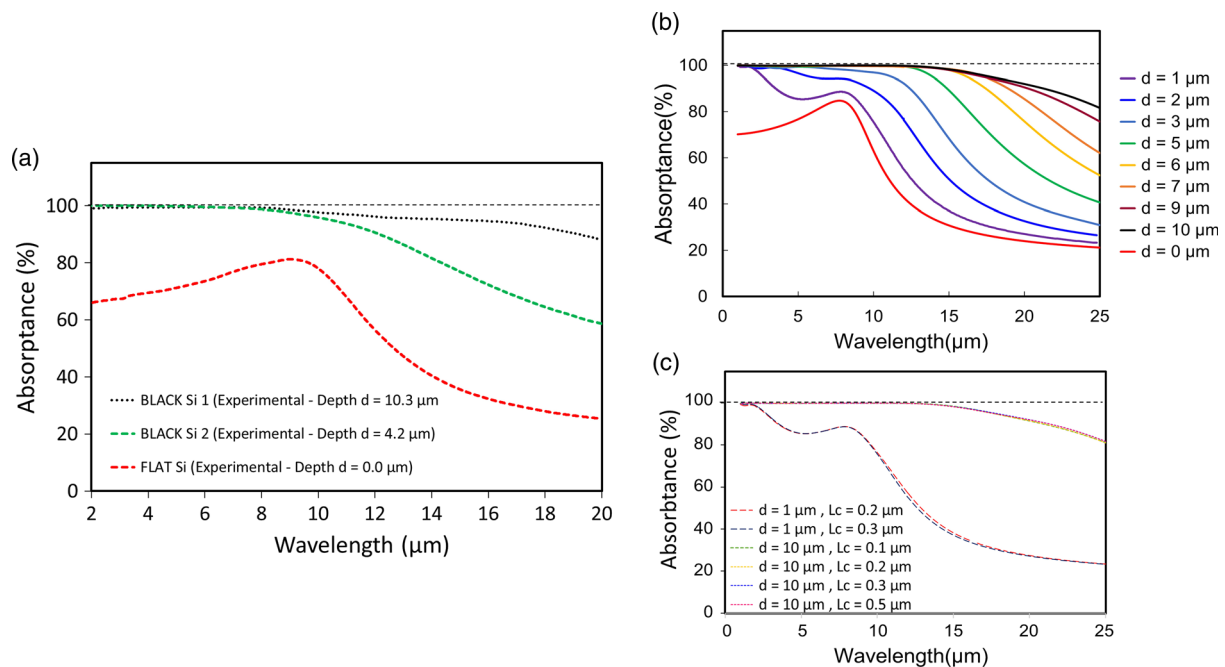


Figure 2. Experimental results and FEM simulations demonstrate the drastic influence of the high aspect ratio through the average depth $\langle d \rangle$ of the conical microstructures. a) Experimentally measured spectral absorptance on three samples of UB-B-Si exhibiting different average depths of $\langle d \rangle = 10.3$, 4.2 , and $0.0 \mu\text{m}$ (flat surface), respectively, recorded at 15° incidence angle. b) Simulated spectral absorptance over the infrared range from 1 to $25 \mu\text{m}$ varying the average depth from $\langle d \rangle = 0 \mu\text{m}$ (flat surface) to $\langle d \rangle = 10 \mu\text{m}$, with 15° incidence angle. c) Simulated spectral absorptance when varying the correlation length (L_c) from 0.1 to $0.5 \mu\text{m}$, showing that this parameter has no observable effect within this sub-wavelength range.

curves meaning that this parameter has no observable effect within this subwavelength range, also corresponding to a condition for applying EMT as discussed afterward.

2.1.2. Effects of Conical Shape and Variability in Tip Depth

To better understand the governing morphological factors, we made another set of simulations, described in **Figure 3a–e**, related to different shapes of the doped silicon surface. In column (I), various shapes of micro/nanostructured (highly doped) silicon are considered for illustration purposes: a flat surface (Figure 3a), periodically arranged uniform nanopillars (Figure 3b), a uniform nanocones array (Figure 3c), and a random distribution of nonuniform nanocones typical of our UB-B-Si (Figure 3d,e). The corresponding profiles of the effective refractive index, derived using the EMT,^[58] are also schematically depicted in columns (II) and (III) of Figure 3. Finally, the simulated spectral absorptance is shown in column (IV). Obtained results clearly show a trend where the smoothest transition of the refractive index is the only configuration which exhibits almost 100% absorptance over the whole spectral range, up to $25 \mu\text{m}$. It is worth mentioning that such smooth transition requires not only conical shapes, but also a high aspect ratio for those cones, which translates into large values of $\langle d \rangle$. Another subtle requirement that is highlighted when comparing Figure 3c,d is the variability in the depths of the tip apex of the cones for obtaining a higher level of absorptance of almost 100%, but at the cost of a slightly shorter bandwidth. This is an

important requirement, which explains the use of an average depth $\langle d \rangle$ instead of a uniform depth d , as one of the most important factors of the morphology besides the conical shape of the nanostructure.

2.1.3. Effect of Correlation Length

At this stage, we have to point out that our analysis based on the smooth transition effective refractive index along the z -axis assumes that the EMT is applicable. Indeed, the main requirement for this is to have subwavelength feature size for the nanostructures in-plane dimensions, to enable averaging the effective refractive index at each z -position. This translates into the condition that the correlation length (L_c) between neighboring cones has to be smaller than the wavelength, that is, $L_c \ll \lambda$. FEM simulations trying to ascertain the effect of the correlation length (L_c) were then performed for the same level of doping and the same cone average depth of $\langle d \rangle = 10 \mu\text{m}$, by varying the correlation length from $L_c = 0.1$ – $0.5 \mu\text{m}$. According to the simulation results shown in Figure 2c, there is only a very little impact of L_c . This result allows us to conclude that the depth $\langle d \rangle$ matters more than the aspect ratio $\langle d \rangle / L_c$ of the conical nanostructures. It is, however, worth mentioning that an additional requirement is subwavelength values for L_c to enable applying the effective medium approximation. From this point-of-view, as shown in **Figure 4III**, typical values of $L_c \approx 0.32$ and $0.44 \mu\text{m}$ for our samples B-Si-1 and B-Si-2 enable us to make this assumption, especially in the infrared range. The corresponding values for the

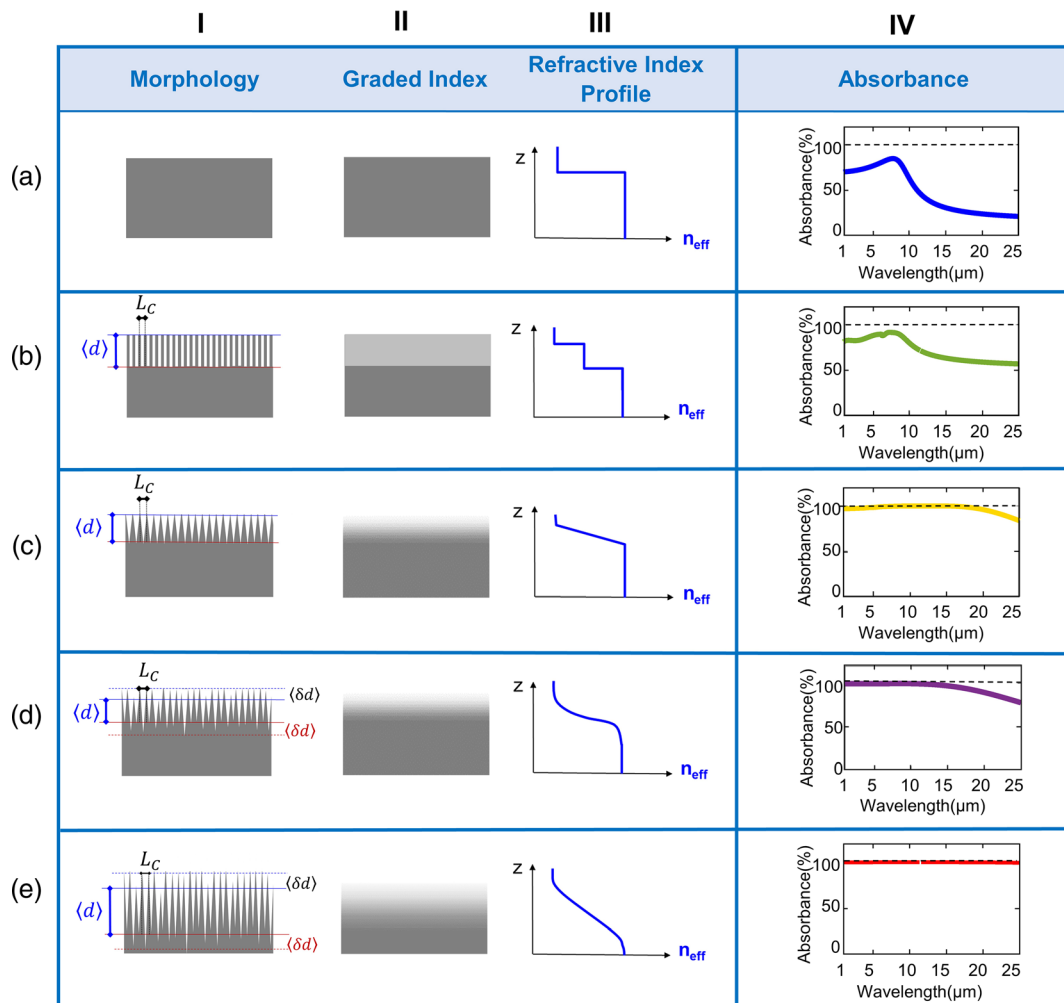


Figure 3. a–e) The high aspect ratio of the conical microstructure as a first key parameter to turn silicon into an ultrabroadband and ultrablack perfect absorber. Schematic representations of different surface geometries (I) along with their corresponding graded index profiles (II) and a sketch of the corresponding profiles of the effective refractive index according to effective medium modeling (III) and the simulated absorptances obtained based on relevant data of our doped silicon (IV). a) Flat silicon. b) Uniform nanopillars array with average depth $\langle d \rangle$ of 5 μm . c) Uniform nanocones array average depth $\langle d \rangle$ of 5 μm . d,e) Nonuniform nanocones array typical of ultrablack silicon with high absorptance having a doping level of nearly $5 \times 10^{19} \text{ cm}^{-3}$ with an average depth $\langle d \rangle$ of 5 and 10 μm , respectively. The latter is the only morphological configuration that exhibits continuous and smooth profile of the refractive index thanks to the stochastic distribution of the cones apex and cone depths (d). Note that the transition from air to bulk silicon will be smoothest in case (e) for the highest average depth $\langle d \rangle$.

average depths are $\langle d \rangle = 10.3 \mu\text{m}$ and $\langle d \rangle = 4.2 \mu\text{m}$, respectively. The method to obtain these data is depicted in Figure 4 and described in Section 4.

2.2. Effect of Doping

Besides the above-described importance of morphology, the second key governing factor is doping. Fundamentally, high doping levels enable tuning the semiconductor to bring it close to a metallic behavior thanks to the increased charge carrier density. From optical point-of-view, silicon becomes a plasmonic material with a plasma frequency in the infrared range, while metals usually exhibit such frequency in the visible domain.^[23] As discussed earlier, silicon can be modelled by a wavelength-dependent complex refractive index based on Drude model, Supporting

Information 3. A second series of simulations were done to provide conclusive evidence of the effect of doping on B-Si for a fixed average depth $\langle d \rangle = 10 \mu\text{m}$. As shown in Figure 5a, with an increasing level of doping, the absorptance increases in the low-wavelength range. In the extreme case of doping, $1 \times 10^{21} \text{ cm}^{-3}$, the absorptance achieves a near 100% level until $\lambda = 5 \mu\text{m}$. However, above $\lambda = 5 \mu\text{m}$, quite the opposite trend is observed; the absorptance decreases while increasing the doping. The inset in Figure 3a is a zoom on the absorptance axis, which depicts key information regarding two different requisites for obtaining broadband silicon absorbers. For a broader high absorptance range, a highly doped silicon is preferable, while for the highest absorptance values, a heavily doped silicon would be ideal. By highly doped levels, we mean levels above to $1 \times 10^{19} \text{ cm}^{-3}$, where we still have significant plasmonic

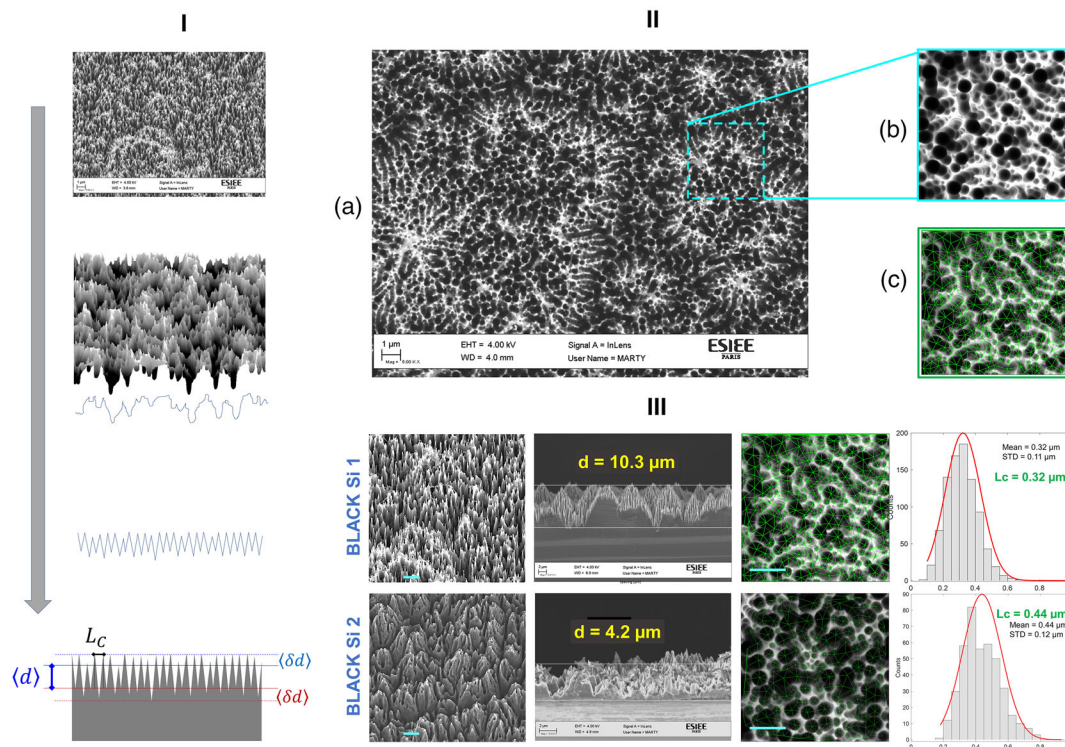


Figure 4. Production of morphology statistics of B-Si using SEM gray-scale analysis. I) Schematic transition from a 3D morphology to a 1D model leading ultimately to the graded refractive index profile required in our work based on topographic information. II) Methodology for obtaining correlation length (L_c) and depth $\langle d \rangle$ from top-view SEM images of B-Si and their exploitation to get statistical data on dimensions and grayscale (see details in Section 4). III) Application to our two samples B-Si-1 and B-Si-2 to retrieve their respective correlation lengths (L_c) and their average depths $\langle d \rangle$.

behavior of the doped silicon. It is worth mentioning that at this particular doping level of $1 \times 10^{19} \text{ cm}^{-3}$, the absorptance starts degrading, reaching levels below 99.6% in the spectral range of interest. This suggests that there is no additional benefit reducing the doping level below this limit. The observed trend observed in Figure 5a on the cutoff wavelengths, which vary with doping, suggests a link with the silicon plasma frequency ω_p , which depends on doping concentration. The corresponding calculated incident wavelength in air, noted λ_p , takes the values $\lambda_p = 4.9$ and 19.6 and $41.6 \mu\text{m}$, respectively, for phosphorous doping concentrations of 1×10^{21} , 4.5×10^{19} , and $1 \times 10^{19} \text{ cm}^{-3}$, respectively. These values of λ_p appear in quite good agreement with the -3 dB cutoff wavelengths, which appear in Figure 5a.

2.3. Effect of Angle of Incidence

The effect of the angle of incidence on the absorptance of silicon has also been investigated, as shown in Figure 5c,d. One can see that the absorptance is nearly isotropic, with almost no dependence on the angle in the range from -40° to $+40^\circ$.

3. Conclusion

In this work, we show through an experimental investigation supported by numerical simulations, the means of turning

silicon into a broadband perfect absorber over the spectral range up to $25 \mu\text{m}$. For this purpose, we use highly doped silicon bulk, at 5×10^{19} phosphorous concentration, to produce black silicon by cryogenic plasma processing of the silicon surface, with sufficient etching time, of 10–20 min, leading to conical nanostructures of very high aspect ratio, up to 30:1, and depth up to $10.3 \mu\text{m}$. Absorptance of 99.5% is achieved in the spectral range up to $8 \mu\text{m}$. It is obtained from indirect method, based on a measured reflectance of 0.5% accounting for both specular and diffuse reflectance, and a transmittance much below 0.005%. Absorptance remains higher than 90% up to a wavelength of $20 \mu\text{m}$. The specific high aspect ratio conical geometrical features of the B-Si surface combined with the high doping of the silicon bulk are a key parameter to understand the outstanding infrared absorptance of B-Si. Our experimental and numerical studies reveal the existence of a trade-off, hence an optimal set of parameters, to obtain both ultrabroadband and ultrablack silicon. Simulation results predict that higher levels of absorptance are obtainable with heavily doped B-Si at 1×10^{20} phosphorous concentration, while broader absorptance could be facilitated by using moderately doped B-Si in the order of $1 \times 10^{19} \text{ cm}^{-3}$. The observed striking behaviors are not only ascribed to the high level of doping of the nanostructured surface, but also to the depth of the conical nanostructures, which is a direct consequence of etching time and to some extent to the doping levels, which has a small influence on morphology. Based on the fact that the

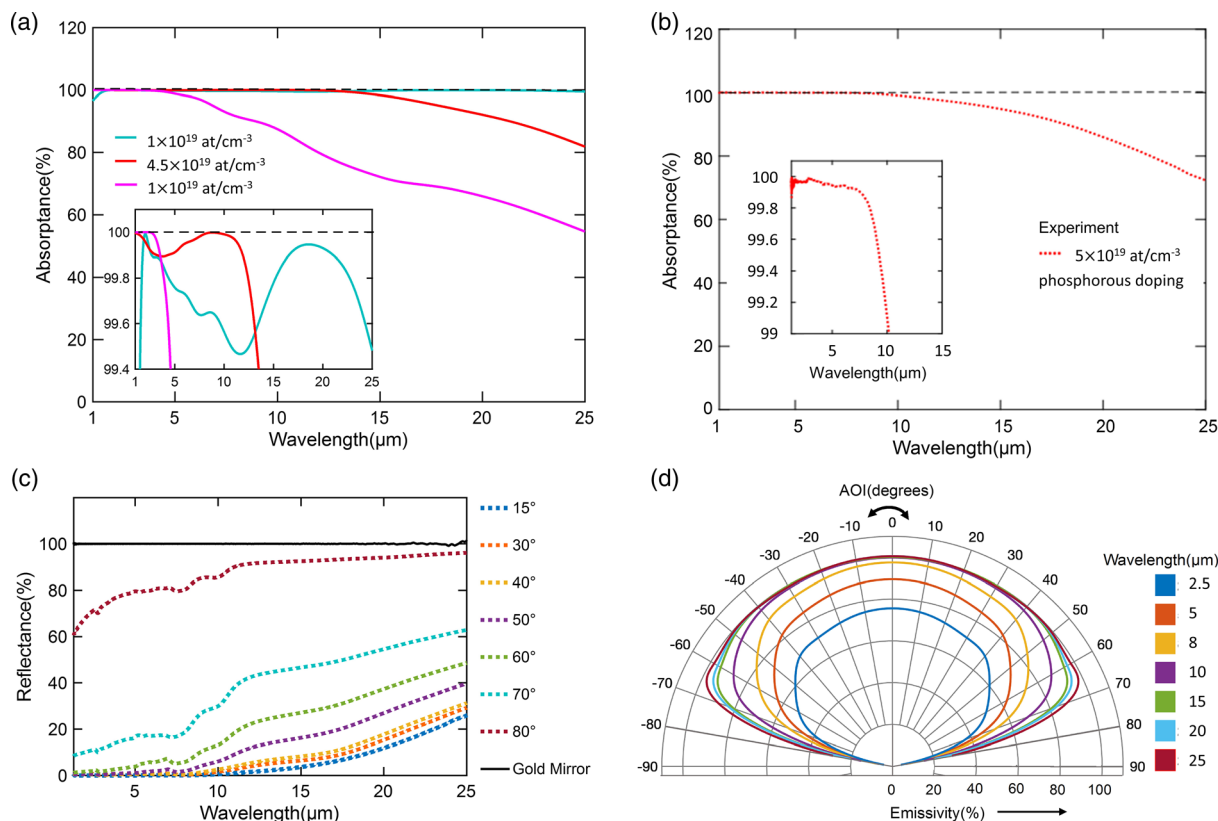


Figure 5. The doping level of silicon as the second key parameter to achieve ultrabroadband and ultrablack silicon. a) Calculated absorptance over the infrared spectral range from 1 to 25 μm for different values of the doping level of N-type, phosphorous-doped silicon with fixed average cone depth $\langle d \rangle = 10 \mu\text{m}$. The inset gives a zoom on the vertical scale to highlight that widest spectral ranges achieved at moderate doping level $1 \times 10^{19} \text{cm}^{-3}$ also correspond to the smallest levels of absorptance, although still high; higher absorptance is attainable at higher doping levels but at the expense of a reduced spectral range. b) Experimental spectral absorptance of black silicon for high ($5 \times 10^{19} \text{cm}^{-2}$) doping level measured over the spectral range from 1 to 25 μm , showing excellent agreement with simulation. c) Reflectance of black silicon for high ($5 \times 10^{19} \text{cm}^{-3}$) doping level measured reflectance at different incident angles, and d) corresponding emissivity diagrams.

absorptance A is derived through the formula $A = i - R - T$, and based on the fact that the measured transmittance T was found to be zero, we can reasonably state that there are two involved mechanisms to ensure an almost perfect absorptance of 100%, as follows: 1) almost no transmission can occur $T \approx 0$ because the thickness ($500 \mu\text{m}$) of the silicon wafer and the corresponding doping level ($5 \times 10^{19} \text{cm}^{-3}$) are both high enough to lead to any residual light to be absorbed within the silicon volume. 2) $R \approx 0$ due to impedance matching involving the tapered structure of the B-Si surface over a depth of $\langle d \rangle = 10 \mu\text{m}$, which is deep enough. In this case, this holds true even at high wavelengths thanks to the high doping of $5 \times 10^{19} \text{cm}^{-3}$. Effects of the angle of incidence and the correlation length of the conical nanostructures have also been explored, and show only to yield small effect on the absorptance of B-Si. The reported exceptionally high absorptance levels in the MIR spectral range also translate into high emissivity of doped B-Si. Such remarkable properties enable considering highly doped and deep B-Si as a propitious candidate for numerous applications, such as radiative cooling, broadband absorbers for IR radiation sensors as well as broadband infrared light sources.

4. Experimental Section

Black Silicon Fabrication: Inductively coupled plasma-reactive ion etching (ICP-RIE), otherwise called deep reactive ion etching (DRIE),^[60,61] is a proven technique allowing dry structuration of silicon surface at different scales in a fast and repeatable manner. While the purported “Bosch” strategy is the most commonly used procedure in DRIE predominantly, however in this work, we have used the cryogenic process developed in our prior report^[3] to obtain the B-Si samples under consideration. The process is carried out in an A601E Alcatel etch tool configured for cryogenic plasma silicon etching at a temperature of $-110 \text{ }^\circ\text{C}$. The B-Si formation process involves plasma generation from a gas mixture of SF_6 and O_2 at a pressure of 2.5 Pa, with detailed formation mechanisms leading to a tapered structure described in our previous work.^[31] By proper control of the SF_6/O_2 ratio, the process leads to the appearance of conical spikes on the silicon surface.^[30] Then further control of the etching time from 10 to 20 min enables the production of the high aspect ratios for these conical structures, which is the key morphological feature for achieving the extraordinary radiative properties presented in this work. The fixed parameters for all examples are ICP intensity of 1000 W and SF_6 gas stream rate of 200 sccm. The samples were delivered on single side polished (100)-oriented single crystalline silicon wafers of 4 in. breadth and $525 \mu\text{m}$ thickness (from Siltronic), with *n*-type phosphorous doping at a measured resistivity of $0.0015 \Omega\text{cm}$, corresponding to a doping

concentration level of $5 \times 10^{19} \text{ cm}^{-3}$. Square samples of 1 cm^2 have been diced upon completion of the plasma process.

Morphology Statistics Generation: SEM gray-scale analysis is a reconstruction technique from which a 3D model that represents the surface topography of B-Si samples can be obtained. This method consists of inferring the structures' depth based on the gray-scale level of a top-view SEM image (Figure 4 and Video S1, Supporting Information), using the known depth values of the SEM brightest and darkest gray-level as bounds of an interpolating range, calibrated from cross-sectional SEM images. While other nondestructive methods of reconstruction such as the ones based on multiple images taken at different viewing angles have been demonstrated, they require repositioning the sample at different viewing angles and robust algorithms to detect the same features in the different images.^[62] SEM gray-scale analysis has been effectively used in the reconstruction of B-Si samples,^[63] however, there are some limitations of the maximum hole depth detectable that are due to the limited SEM dynamical range. Therefore, while the SEM gray-scale analysis provides accurate topography information, it is limited to B-Si samples with small or medium aspect ratios. In this work, as schematically depicted in Figure 5, from both top- and side-view SEM pictures, the nanocones coherence length L_c and the average nanocones depth $\langle d \rangle$ of the B-Si structures have been extracted by gray-level analysis using MATLAB: all the centers of holes have been identified and each pixel corresponds to a depth. The obtained results demonstrate a correlation length ranging from $L_c \approx 0.44 \mu\text{m}$ down to $L_c \approx 0.32 \mu\text{m}$.

Experimental Setup for Measurements of Reflectance: Experimental measurements of transmissivity and specular reflectivity have been performed using a Perkin Elmer Spectrum Two FT-IR Spectrometer in the MIR and far-infrared spectral ranges from 1 to $25 \mu\text{m}$ at room temperature. Measurements at near-normal incidence have been obtained with a specular reflectance accessory with an incidence angle of 10° . A variable angle specular reflectance accessory has also been used to perform measurements at different angles of incidence from 15° to 80° . The diffuse reflectance measurements were performed using a PerkinElmer Spectrum 3 FT-IR spectrometer with a PIKE IntegratIR MIR Integrating Sphere having hemispherical diffuse reflectance measurement with an incident beam angle of 12° with specular exclusion port from PIKE Technologies at room temperature in the spectral range from 2.5 to $20 \mu\text{m}$. Cumulative measurements on flat silicon with standard low and high doping levels have also been performed for comparison. We measured absorbance on two fabricated B-Si-1 and B-Si-2 samples having two different average depths $\langle d \rangle = 10.3 \mu\text{m}$ and $\langle d \rangle = 4.2 \mu\text{m}$, respectively. The measured absorbance A is obtained indirectly from the measured reflectance R and transmittance T , through $A = 1 - R - T$, where R accounts for both specular reflectance (R_{spec}) and diffuse reflectance (R_{diff}), that is, $R = R_{\text{spec}} + R_{\text{diff}}$ as shown in Figure 1d,e. T appeared to have very negligible, nonobservable values over the whole spectral range (inset of Figure 1d), which is understandable because light is transmitted (and attenuated) over the whole silicon substrate, whose thickness is $525 \mu\text{m}$.

Supporting Information

Supporting Information is available from the Wiley Online Library or from the author.

Acknowledgements

This work was supported by the I-SITE FUTURE Initiative (Reference ANR-16-IDEX-0003) and by the METAWATER Project (No. 1036 ANR-20-CE08-0023 META-WATER) from Agence Nationale de la Recherche (ANR), France.

Conflict of Interest

The authors declare no conflict of interest.

Author Contributions

T.B. initiated the project together with Y.-M.S. and in collaboration with Z.-Z.L. T.B. designed the experiments and supervised writing of the manuscript. S.S. and A.A.E. have equal contribution as part of their Ph.D. work, mainly for conducting numerical simulations under the guidance of E.R. and Y.-M.S., respectively. P.B., E.N., and T.B. supervised the work conducted by S.S. P.B. was also responsible for SEM analysis. E.N. was also responsible for the measurement of the spectral responses, with contributions from J.D., X.L., and S.S. Fabrication of the samples was done by F.M. with contributions from T.B. and P.B. All authors discussed the results. E.N., P.B., S.S., X.L., and T.B. revised the manuscript. S.S. and A.A.E. contributed equally to this work.

Data Availability Statement

The data that support the findings of this study are available from the corresponding author upon reasonable request.

Keywords

conical nanostructurations, highly doped silicon, mid-infrared metamaterials, perfect light absorbers, ultrablack silicon, ultrabroadband absorbers

Received: August 5, 2022

Revised: October 13, 2022

Published online: October 30, 2022

- [1] M. Beard, J. Luther, A. Nozik, *Nat. Nanotech.* **2014**, *9*, 951.
- [2] J. H. Oh, H. C. Yuan, H. M. Branz, *Nat. Nanotech.* **2012**, *7*, 743.
- [3] H. Savin, P. Repo, G. von Gastrow, P. Ortega, E. Calle, M. Garin, R. Alcubilla, *Nat. Nanotech.* **2015**, *10*, 624.
- [4] G. Smith, A. Gentle, *Nat. Energy* **2017**, *2*, 17142.
- [5] A. P. Raman, M. A. Anoma, L. X. Zhu, E. Rephaeli, S. H. Fan, *Nature* **2014**, *515*, 540.
- [6] N. N. Shi, C. C. Tsai, F. Camino, G. D. Bernard, N. F. Yu, R. Wehner, *Science* **2015**, *349*, 298.
- [7] B. Zhao, M. K. Hu, X. Z. Ao, N. Chen, G. Pei, *Appl. Energy* **2019**, *236*, 489.
- [8] D. G. Baranov, Y. Xiao, I. A. Nechepurenko, A. Krasnok, A. Alù, M. A. Kats, *Nat. Mater.* **2019**, *18*, 920.
- [9] Z. J. Coppens, J. G. Valentine, *Adv. Mater.* **2017**, *29*, 1701275.
- [10] M. A. Juntunen, J. Heinonen, V. Vähänissi, P. Repo, D. Valluru, H. Savin, *Nat. Photon.* **2016**, *10*, 777.
- [11] Z. H. Huang, J. E. Carey, M. G. Liu, X. Y. Guo, E. Mazur, J. C. Campbell, *Appl. Phys. Lett.* **2006**, *89*, 033506.
- [12] G. Mi, J. Lv, L. Que, Y. Zhang, Y. Zhou, Z. Y. Liu, *Nanoscale Res. Lett.* **2021**, *16*, 38.
- [13] Y. Zhou, Z. Qin, Z. Liang, D. Meng, H. Xu, D. R. Smith, Y. Liu, *Light Sci. Appl.* **2021**, *10*, 138.
- [14] J. Tao, Z. Liang, G. Zeng, D. Meng, D. R. Smith, Q. H. Liu, Q. Yang, M. Zhang, W. Pang, J. Liang, T. Bourouina, *Nanophotonics* **2020**, *10*, 1337.
- [15] Y. Luo, D. Meng, Z. Liang, J. Tao, J. Liang, C. Chen, J. Lai, T. Bourouina, Y. Qin, J. Lv, Y. Zhang, *Opt. Commun.* **2020**, *459*, 124948.
- [16] G. Kirchhoff, *Annal. Phys. Chem.* **1860**, *109*, 275.
- [17] K. Q. Peng, S. T. Lee, *Adv. Mater.* **2011**, *23*, 198.
- [18] S. Basu, L. Wang, *Appl. Phys. Lett.* **2013**, *102*, 053101.
- [19] X. L. Liu, L. P. Wang, Z. M. Zhang, *J. Heat Transfer.* **2013**, *135*, 061602.

- [20] P. Yu, J. Wu, S. Liu, J. Xiong, C. Jagadish, Z. M. Wang, *Nano Today* **2016**, *11*, 704.
- [21] T. H. Her, R. J. Finlay, C. Wu, S. Deliwala, E. Mazur, *Appl. Phys. Lett.* **1998**, *73*, 1673.
- [22] C. Wu, C. H. Crouch, L. Zhao, J. E. Carey, R. Younkin, J. A. Levinson, E. Mazur, *Appl. Phys. Lett.* **2001**, *78*, 1850.
- [23] R. Younkin, J. E. Carey, E. Mazur, J. A. Levinson, C. M. Friend, *J. Appl. Phys.* **2003**, *93*, 2626.
- [24] C. H. Crouch, J. E. Carey, M. Shen, E. Mazur, F. Y. Génin, *Appl. Phys. A* **2004**, *79*, 1635.
- [25] S. Kontermann, T. Gimpel, A. Baumann, K.-M. Guenther, W. Schade, *Energy Proc.* **2012**, *27*, 390.
- [26] Y. Ma, H. Ren, J. Si, X. Sun, H. Shi, T. Chen, F. Chen, X. Hou, *Appl. Surf. Sci.* **2012**, *261*, 722.
- [27] C. H. Li, J. H. Zhao, X. Y. Yu, Q. D. Chen, J. Feng, H. B. Sun, *IEEE Photonics J.* **2016**, *8*, 1.
- [28] A. Y. Vorobyev, C. Guo, *Laser Photon. Rev.* **2013**, *7*, 385.
- [29] H. Jansen, M. de Boer, R. Legtenberg, M. Elwenspoek, *J. Micromech. Microeng.* **1995**, *5*, 115.
- [30] K. N. Nguyen, P. Basset, F. Marty, Y. Leprince-Wang, T. Bourouina, *J. Appl. Phys.* **2013**, *113*, 194903.
- [31] D. Abi Saab, P. Basset, M. J. Pierotti, M. L. Trawick, D. E. Angelescu, *Phys. Rev. Lett.* **2014**, *113*, 265502.
- [32] M. Steglich, D. Lehr, S. Ratzsch, T. Käsebier, F. Schrempel, E.-B. Kley, A. Tünnermann, *Laser Photon. Rev.* **2014**, *8*, L13.
- [33] M. Steglich, T. Käsebier, M. Zilk, T. Pertsch, E.-B. Kley, A. Tünnermann, *J. Appl. Phys.* **2014**, *116*, 173503.
- [34] J. Lv, T. Zhang, P. Zhang, Y. Zhao, S. Li, *Nanoscale Res. Lett.* **2018**, *13*, 110.
- [35] X. Liu, P. R. Coxon, M. Peters, B. Hoex, J. M. Cole, D. J. Fray, *Energy Environ. Sci.* **2014**, *7*, 3223.
- [36] C. H. Hsu, J. R. Wu, Y. T. Lu, D. J. Flood, A. R. Barron, L. C. Chen, *Mat. Sci. Semicon.* **2014**, *25*, 2.
- [37] M. Otto, H. Algasinger, B. Branz, T. Gesemann, K. Gimpel, T. Fuchsel, S. Kasebier, S. Kontermann, S. Koynov, X. Li, V. Naumann, J. Oh, A. N. Sprafke, J. Ziegler, M. Zilk, R. B. Wehrspohn, *Adv. Opt. Mater.* **2015**, *3*, 147.
- [38] Y. C. Wang, J. S. Gao, H. G. Yang, X. Y. Wang, *J. Mater. Sci.: Mater. Electron.* **2016**, *27*, 9002.
- [39] Y. L. Wang, S. Y. Liu, Y. Wang, G. J. Feng, J. T. Zhu, L. Zhao, *Mater. Lett.* **2009**, *63*, 2718.
- [40] P. Repo, A. Haarahiltunen, L. Sainiemi, M. Yli-Koski, H. Talvitie, M. C. Schubert, H. Savin, *IEEE J. Photovolt.* **2012**, *3*, 90.
- [41] M. Algasinger, J. Paye, F. Werner, J. Schmidt, M. S. Brandt, M. Stutzmann, S. Koynov, *Adv. Energy Mater.* **2013**, *3*, 1068.
- [42] H. M. Branz, V. E. Yost, S. Ward, K. M. Jones, B. To, P. Stradins, *Appl. Phys. Lett.* **2009**, *94*, 231121.
- [43] J. Pezoldt, T. Kups, M. Stubenrauch, M. Fischer, *Phys. Status Solidi C* **2011**, *8*, 1021.
- [44] F. Atteia, J. Le Rouzo, L. Denaix, D. Duc, G. Berginc, J. J. Simon, L. Escoubas, *Mat. Res. Bull.* **2020**, *131*, 110973.
- [45] D. Yurasov, A. Novikov, M. Shaleev, N. Baidakova, E. Morozova, E. Skorokhodov, Y. Ota, A. Hombe, Y. Kurokawa, N. Usami, *Mat. Sci. Semicond.* **2018**, *75*, 143.
- [46] B. R. Tull, M. T. Winkler, E. Mazur, *Appl. Phys. A* **2009**, *96*, 327.
- [47] Y. Liu, S. Liu, Y. Wang, G. Feng, J. Zhu, L. Zhao, *Laser Phys.* **2008**, *18*, 1148.
- [48] P. G. Maloney, P. Smith, V. King, C. Billman, M. Winkler, E. Mazur, *Appl. Opt.* **2010**, *49*, 1065.
- [49] Y. Song, T. Liu, S. Liu, J. Huang, J. Li, C. Tian, T. Yu, Y. He, Y. Liu, Z. Zhong, *J. Mater. Sci.: Mater. Electron.* **2020**, *31*, 4696.
- [50] K. Wang, J. S. Gao, H. G. Yang, X. Y. Wang, Y. C. Wang, Z. Zhang, *Appl. Surf. Sci.* **2019**, *464*, 502.
- [51] A. F. Cihan, A. G. Curto, S. Raza, P. G. Kik, M. L. Brongersma, *Nat. Photon.* **2018**, *12*, 284.
- [52] H. Lin, B. C. P. Sturmberg, K. T. Lin, Y. Yang, X. Zheng, T. K. Chong, C. M. de Sterke, B. Jia, *Nat. Photon.* **2019**, *13*, 270.
- [53] L. Zhou, Y. Tan, J. Wang, W. Xu, Y. Yuan, W. Cai, S. Zhu, J. Zhu, *Nat. Photon.* **2016**, *10*, 393.
- [54] L. Zhou, Y. Tan, D. Ji, B. Zhu, P. Zhanh, J. Xu, Q. Gan, Z. Yu, J. Zhu, *Sci. Adv.* **2016**, *8*, E150122.
- [55] H. Zhu, F. Yi, E. Cubukcu, *Nat. Photon.* **2016**, *10*, 709.
- [56] Y. B. Chen, Z. M. Zhang, *J. Phys. D: Appl. Phys.* **2008**, *41*, 095406.
- [57] G. V. Naik, V. M. Shalaev, A. Boltasseva, *Adv. Mater.* **2013**, *25*, 3264.
- [58] T. C. Choy, in *Effective Medium Theory: Principles and Applications*, Vol. 165, Oxford University Press, Oxford, UK **2015**.
- [59] A. A. Elsayed, Y. M. Sabry, F. Marty, T. Bourouina, D. Khalil, *Opt. Express* **2018**, *26*, 13443.
- [60] F. Marty, L. Rousseau, B. Saadany, B. Mercier, O. Français, Y. Mita, T. Bourouina, *Microelectron. J.* **2005**, *36*, 673.
- [61] J. Parasuraman, A. Summanwar, F. Marty, P. Basset, D. Angelescu, T. Bourouina, *Microelectron. Eng.* **2014**, *113*, 35.
- [62] J. Stampfl, S. Scherer, M. Gruber, O. Kolednik, *Appl. Phys. A* **1996**, *63*, 341.
- [63] F. Y. Zhu, Q. Q. Wang, X. S. Zhang, W. Hu, X. Zhao, H. Zhang, *Nanotechnology*, **2014**, *25*, 185705.